Title

Practical aspects of diffractive imaging using an atomic-scale coherent electron probe

Authors

Chen, Z

Weyland, M

Ercius, P

et al.

Publication Date

2016-10-01

DOI

10.1016/j.ultramic.2016.06.009

Peer reviewed

Ultramicroscopy 169 (2016) 107–121

Contents lists available at ScienceDirect

Ultramicroscopy

journal homepage: www.elsevier.com/locate/ultramic

Practical aspects of diffractive imaging using an atomic-scale coherent electron probe

Z. Chen [a,*], M. Weyland [b,c], P. Ercius [d], J. Ciston [d], C. Zheng [a,e], M.S. Fuhrer [a], A.J. D'Alfonso [f], L.J. Allen [f], S.D. Findlay [a]

[a] School of Physics and Astronomy, Monash University, Clayton, Victoria 3800, Australia
[b] Monash Centre for Electron Microscopy, Monash University, Clayton, Victoria 3800, Australia
[c] Department of Materials Science and Engineering, Monash University, Clayton, Victoria 3800, Australia
[d] National Center for Electron Microscopy, Molecular Foundry, Lawrence Berkeley National Laboratory, Berkeley, CA 94720, USA
[e] Department of Civil Engineering, Monash University, Clayton, Victoria 3800, Australia
[f] School of Physics, University of Melbourne, Parkville, Victoria 3010, Australia

ARTICLE INFO

Article history:
Received 14 April 2016
Received in revised form
16 June 2016
Accepted 23 June 2016
Available online 25 June 2016

Keywords:
Diffractive imaging
Convergent beam electron diffraction
Differential phase contrast
Phase reconstruction

ABSTRACT

Four-dimensional scanning transmission electron microscopy (4D-STEM) is a technique where a full two-dimensional convergent beam electron diffraction (CBED) pattern is acquired at every STEM pixel scanned. Capturing the full diffraction pattern provides a rich dataset that potentially contains more information about the specimen than is contained in conventional imaging modes using conventional integrating detectors. Using 4D datasets in STEM from two specimens, monolayer MoS_2 and bulk $SrTiO_3$, we demonstrate multiple STEM imaging modes on a quantitative absolute intensity scale, including phase reconstruction of the transmission function via differential phase contrast imaging. Practical issues about sampling (i.e. number of detector pixels), signal-to-noise enhancement and data reduction of large 4D-STEM datasets are emphasized.

1. Introduction

Convergent beam electron diffraction (CBED) patterns acquired using an atomic size coherent probe in scanning transmission electron microscopy (STEM) contain rich structural information. However, traditional STEM experiments such as bright field (BF) or annular dark field (ADF) use monolithic detectors that integrate over many points in the diffraction plane to allow fast acquisition and high signal-to-noise ratio (SNR). Though position-resolved electron diffraction has a long history [1–3], the slow readout speed of the conventional CCD camera, limited data transfer speed and limited storage space have restricted acquisition to a small number of frames, making atomic resolution diffractive imaging extremely challenging [4]. Recent developments in fast-readout pixel detectors and powerful computers significantly improve the speed of data acquisition and transfer, and make possible the acquisition of two-dimensional CBED patterns with two dimensional probe scanning positions – a four dimensional (4D) dataset – at atomic resolution [5–7]. Such 4D datasets have been shown to allow synthesizing multiple imaging modes [4,8], differential phase contrast imaging [6] and ptychographic phase reconstruction [7,9]. However, the full potential of 4D datasets for quantitative analysis has yet to be established. The huge size of the 4D datasets also makes data storage, transfer and analysis challenging. Therefore, approaches to reducing the data size while conserving the information of interest are highly desirable.

In this paper, we demonstrate quantitative imaging on an absolute intensity scale for both coherent and incoherent STEM image modes, including differential phase contrast imaging and quantitative phase reconstruction. Practical experimental considerations, such as detector extent and sampling (i.e. number of detector pixels), SNR and information content are also discussed with a view to providing guidelines for future experiments.

2. Experimental methods and data processing

The experiments were carried out on the TEAM I electron microscope at the National Center for Electron Microscopy (NCEM) facility of the Molecular Foundry in Berkeley, California, operating at 300 kV. Using an atomic size probe, CBED patterns were acquired at each probe position using a Gatan K2-IS direct detection camera operated in a linear mode at 400 frames per second. Each CBED pattern has 1920×1792 pixels and patterns with up to

* Corresponding author.
E-mail address: zhen.chen@monash.edu (Z. Chen).

http://dx.doi.org/10.1016/j.ultramic.2016.06.009
0304-3991/

256 × 256 scanning probe positions were acquired, giving raw datasets of several hundred gigabytes (GBs). The data were first distilled into *.dm4 format files from the raw binary data using the Gatan in situ imaging plugin. The *.dm4 files were then read into MATLAB using an efficient and fast script [10]. The default MATLAB file (*.mat), an HDF5-based format storing the data in compressed chunks, was used in the following data analysis employing custom MATLAB codes. To treat huge datasets – several hundred GBs in size, much larger than the random-access memory installed in most computers – the datasets were loaded into the memory sequentially, facilitated by the fast read and write speed of the solid state disks (SSDs) (in our case quad striped PCIe bus SSDs). Reading and writing in data stacks instead of single frames or pixels was used to reduce the reading and writing times and accelerate the data analysis.

Two materials were chosen in this study, monolayer MoS_2 and bulk $SrTiO_3$. Monolayer MoS_2 is a weakly scattering material, making it suitable for differential phase contrast imaging since the phase-object approximation is expected to be satisfied. $SrTiO_3$ is a well-known perovskite structure with both light and heavy atomic columns and is widely used for testing new imaging techniques, making it a suitable test case for exploring quantitative imaging from a variety of imaging modes. The experiments on MoS_2 used a convergence semi-angle of $\alpha = 17.1$ mrad which, for an ideally coherent probe, corresponds to a diffraction limited probe size of 1.1 Å, and a beam current of about 48 pA, as read from the viewing screen which was calibrated using the drift tube of a Gatan spectrometer. The experiments on $SrTiO_3$ used $\alpha = 21.3$ mrad (probe size 0.9 Å) and a beam current of about 65 pA, with data taken from multiple areas of differing thickness. A high-angle annular dark-field (HAADF) image was acquired simultaneously with the 4D datasets. HAADF images before and after the 4D dataset acquisition were also taken to monitor the beam damage: only those datasets with modest change between before and after HAADF images were chosen for the data analysis.

The thicknesses of the different regions of $SrTiO_3$ examined were determined by the L^2-norm method [11,12] from the position averaged CBED (PACBED) pattern obtained by averaging the 4D dataset. A two-dimensional (2D) Gaussian function was assumed to account for the spatial incoherence, taken to include both the effective source size and additional broadening introduced by the repeat unit averaging procedure (discussed below) used to correct specimen drift and improve SNR. The Gaussian width was determined by comparing the averaged experimental HAADF images acquired simultaneously with the 4D dataset acquisition with HAADF images simulated using the quantum excitation of phonons method implemented in the software μSTEM [13,14]. The half-width half-maximum (HWHM) thus determined is approximately 0.45 Å for MoS_2 and 0.50 Å for $SrTiO_3$. The incident beam intensity for image normalization was measured by taking one aperture image in vacuum for each experimental condition using the same camera. In the case of $SrTiO_3$, there was some evidence of variation of the beam current during experiments, which was attributed to monochromator settings or gun alignment change. To compensate for this, a single multiplicative factor of 0.86 was applied to all $SrTiO_3$ datasets prior to quantitative image comparison with the simulations. This factor is consistent with the difference between the total integrated intensity of the whole PACBED pattern of each dataset (scattering angle up to 4α for $SrTiO_3$) and the total intensity from the aperture image in vacuum, to within the uncertainty introduced by the relatively large variations of the dark current reference and weak SNR at high scattering angles in the CBED patterns. (Note that simulations show the percentage of electron intensity scattered outside the scattering angle of 4α is less than 1% for even the thicker specimen region considered.).

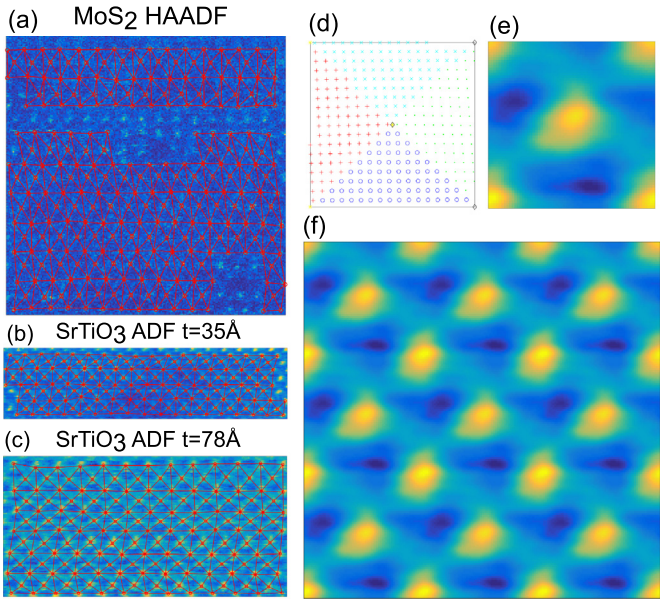

Fig. 1. Raw images used for scanning drift correction: (a) HAADF image of MoS_2 acquired simultaneously with the 4D dataset; (b) and (c) synthesized ADF images for a 35 Å and 78 Å thick region of $SrTiO_3$ respectively. The circles indicate the column positions and the lines show the triangular patches. (d) The coordinates of the image pixels after the affine transformation of a single unit-cell area patch in (c). (e) Averaged unit-cell image for the 78 Å thick region of $SrTiO_3$. (f) A 3 × 3 unit-cell tiling of the image in (e) for visualization purposes. (For interpretation of the references to color in this figure caption, the reader is referred to the web version of this paper.).

Whereas conventional HAADF STEM imaging is carried out with a dwell time on the order of tens of microseconds, acquisition of the full diffraction patterns on the K2-IS camera necessitated a dwell time of 2.5 ms per pixel, a much slower scan. Consequently, specimen drift becomes a substantial problem. In addition, the fine pixel size in the CBED patterns means a poor SNR at each individual pixel. Using the simultaneously acquired HAADF image (or a suitably robust synthesized image) as a structural reference, shown in Fig. 1(a)–(c), the known structure of MoS_2 and $SrTiO_3$ was used to correct scanning drift via a local geometric image transformation method [15]. The main steps in this method are as follows. A normalized cross-correlation method is used to determine the coordinates of the atomic column positions. Next, the reference image is partitioned into a disjoint triangular mesh with these column positions as vertices: nearest neighbor Sr–Sr–Ti triangles in $SrTiO_3$ and Mo–Mo–Mo triangles in MoS_2. The red lines overlaid onto the images shown in Fig. 1(a)–(c) illustrate the triangular patches. The evidently damaged areas in the MoS_2 specimen were not included during the averaging procedure. For each triangle, an affine transformation matrix is then defined that maps the three vertices from the reference image to their expected configuration based on the known model structure. An example of the coordinates of the image pixels after the affine transformation of one unit-cell area from Fig. 1(c) is shown in Fig. 1(d). The transformation matrix thus set up is then applied to map each experimental point within each triangular template to a fractional coordinate $\mathbf{R}_j$ within the unit cell. Due to specimen drift and sampling, the set of positions $\{\mathbf{R}_j\}$ thus defined is not on a regular mesh and so cannot readily be visualized. However, based on the periodicity of the crystal structure, the measured STEM image intensities at the points $\mathbf{R}_j$ can be related to the Fourier coefficients of the STEM image $I_{\mathbf{G}}$ via

$$I(\mathbf{R}_j) = \sum_{\mathbf{G}} I_{\mathbf{G}} e^{2\pi i \mathbf{R}_j \cdot \mathbf{G}}. \quad (1)$$

Since large areas with many unit cells were acquired in our raw datasets, the measured experimental data at all the new coordinates $\mathbf{R}_j$ in Eq. (1) constitutes an overdetermined set of linear equations for the Fourier coefficients $I_{\mathbf{G}}$, which were solved using singular value decomposition. Finally, the $I_{\mathbf{G}}$ thus determined can be used to reconstruct an averaged real space image at any desired scanning sampling. Fig. 1(e) shows the resultant averaged ADF unit-cell image of the raw data in Fig. 1(c). For visualization purposes, the 3×3 tiling of this averaged cell is shown in Fig. 1(f). This procedure can be applied separately to each pixel position in the CBED pattern to reconstruct an "averaged" 4D dataset appropriate to a single unit cell. As will be shown, this Fourier averaging largely corrects for scanning drift and significantly improves the SNR of the diffraction patterns. In principle, this method can also be applied to periodic samples of unknown structure provided a good structural template, such as a fast scan image without significant drift, is available.

3. Quantitative imaging from 4D datasets

With the full 2D CBED patterns at every pixel, any shape and size of a virtual image detector can be formed digitally [4,8,16]. Synthesizing conventional STEM images is a good starting point for further data analysis, allowing the quality of the 4D datasets to be evaluated. Questions on the sensitivity [17] and quantum efficiency [18] have been explored for pixel direct detection cameras, but their use for absolute-scale quantitative imaging in STEM has received less attention. Contrast mismatch or "Stobbs factor" issues in TEM have been discussed since the 1990s [19]. Recently, different imaging modes have been achieved on an absolute intensity scale in high-resolution TEM [20], and both HAADF [21] and BF [22] STEM. Compared with the challenges in determining detailed response of integrating detectors [23], pixel detectors should provide a fast route to absolute-scale imaging. Establishing this is a necessary first step in developing confidence in using the new detector for quantitative analysis.

Here we synthesized low-angle annular dark field (ADF, α-2α), incoherent bright field (BF, 0-α), annular bright field (ABF, collection angle $\frac{\alpha}{2}$-α), and central small bright field (cBF4, $0-\frac{\alpha}{4}$ or cBF10, $0-\frac{\alpha}{10}$) images. Such images are shown in Fig. 2 for MoS_2 (excepting ADF, as the SNR for this weakly scattering sample is too low to give a reliable image), and Figs. 3 and 4 for regions of 35 Å and 78 Å thick $SrTiO_3$ respectively. The images are normalized by the incident beam current and shown as a fractional intensity of the incident beam. In Fig. 2(b)–(d), both Mo and S atoms can be seen clearly, even in this weakly scattering monolayer material.

The simulations used the quantum excitation of phonons method [13] with 20 phonon configurations. As has been established [24], obtaining quantitative agreement between experiment and simulation requires careful characterization of the experiment and detailed simulations. Due to the aberration correction of the probe-forming lens, it generally suffices to model the aberration-corrected lens as being aberration-free. We therefore ignore all the aberration coefficients except for spherical aberration (C_s) and defocus. We used $C_s = 1$ μm to model a small residual C_s. As coherent bright field images are sensitive to defocus, the contrast – defined as the ratio between standard deviation and mean intensity – of the cBF4 image for MoS_2 and the cBF10 image for $SrTiO_3$ was used to estimate defocus, giving −50 Å for MoS_2, −30 Å for the 35 Å thick region of $SrTiO_3$, and −20 Å for the 78 Å region $SrTiO_3$. In conventional high-resolution TEM imaging, two-dimensional image fitting is often used to determine/refine the imaging conditions (e.g. Ref. [47]). However, we find that the asymmetric features in the images in Figs. 3(d) and 4(d) – attributed to a mix of asymmetric lens aberrations, sample mistilt and scan noise – hamper such an approach, making it less convincing than the fit based on simple image contrast. Analysis of the absolute intensity of the S columns in the images in Fig. 2 revealed that approximately 50% of the sulfur atoms were sputtered due to beam irradiation. The intensity on sulfur positions varies at

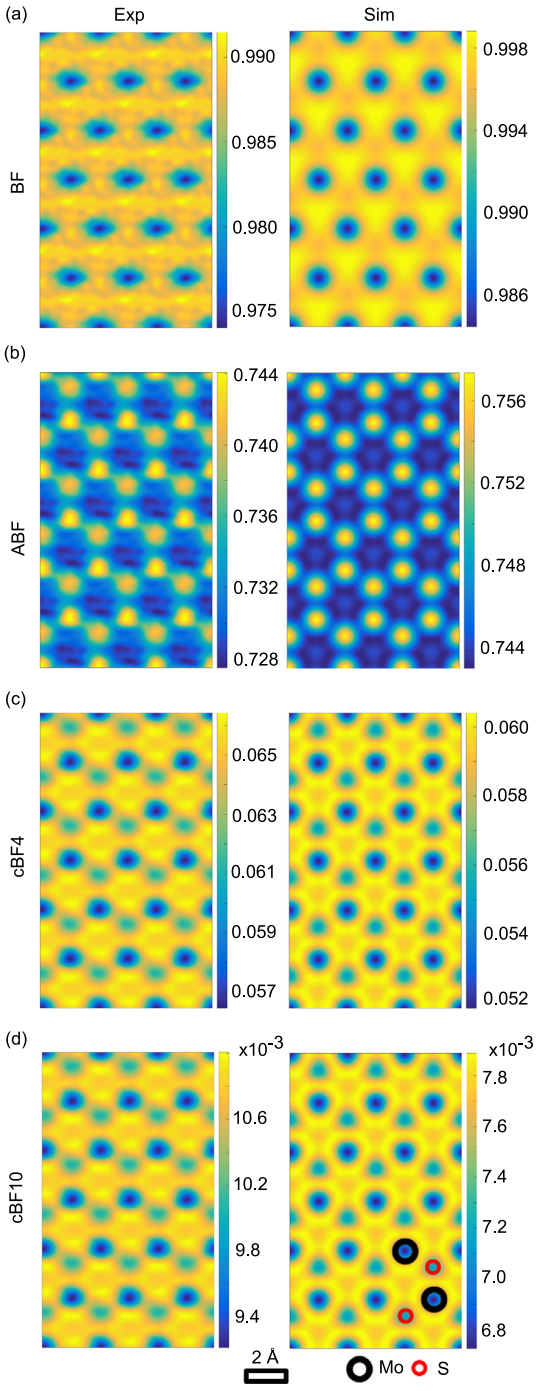

Fig. 2. Synthesized image modes for MoS_2, from a probe convergence semi-angle $\alpha = 17.1$ mrad. (a) Incoherent bright-field (BF), collection angle 0–α; (b) annular bright-field (ABF), collection angle $\frac{\alpha}{2} - \alpha$; (c) coherent bright-field (cBF4), collection angle $0 - \frac{\alpha}{4}$; (d) coherent bright-field (cBF10), collection angle $0 - \frac{\alpha}{10}$. Experimental images are given in the left column, simulation in the right. The intensity scale is given in units of fractional intensity of the incident beam. For clear visualization of the structure in these low-contrast images, experimental and simulated images are shown on separate scales. Quantitative comparison reveals the ranges to be comparable, and the difference in means, while comparable to the narrow range, to be both a very small fraction of that mean and of a size consistent with the uncertainty in dark current subtraction. The simulations shown used a structural model with one sulfur layer.

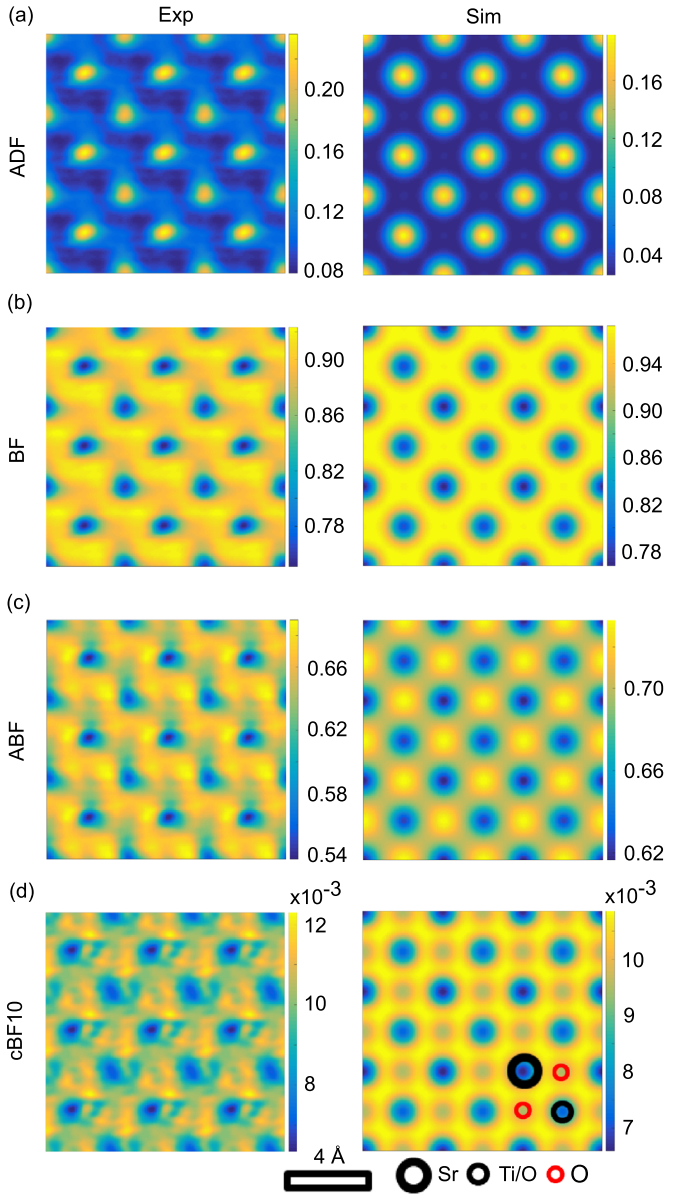

Fig. 3. Synthesized image modes for a 35 Å thick region of $SrTiO_3$, from a probe convergence semi-angle $\alpha = 21.3$ mrad. (a) Annular dark-field (ADF), collection angle $\alpha - 2\alpha$; (b) incoherent bright-field (BF), collection angle 0-α; (c) annular bright-field (ABF), collection angle $\frac{\alpha}{2} - \alpha$; (d) coherent bright-field (cBF10), collection angle $0 - \frac{\alpha}{10}$. Experimental images are given in the left column, simulation in the right. The intensity scale is given in units of fractional intensity of the incident beam.

different probe positions in the raw image, which can be seen clearly in the HAADF images taken simultaneously with the 4D dataset (not shown) and the synthesized coherent bright field images (discussed later in Fig. 7(d)). After repeat unit average processing, there is approximately one sulfur atom per projected sulfur site in the unit cell. The mechanism of the chemical stability of this largely defective MoS_2 requires further study, but a high degree of sputtering is expected since the 300 kV high voltage used is much higher than the electron threshold potential of MoS_2 (90 kV, Ref. [25]) and the sputtering cross-section of sulfur atoms with the dose of 7.5×10^5 e^- per probe position is estimated to be about 0.26 sulfur atoms per probe position on average, as discussed in detail in Ref. [26] in connection to a similar dataset. All the MoS_2 simulations in this manuscript, including those in Fig. 2, therefore used a structural model with one sulfur layer.

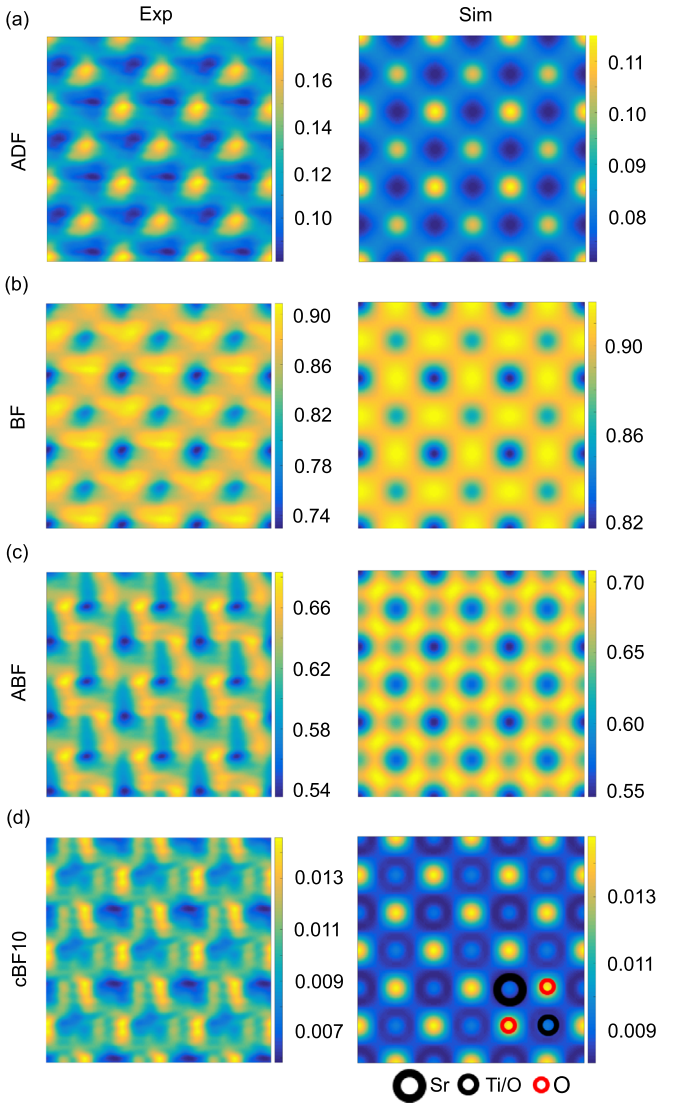

Fig. 4. Synthesized image modes for a 78 Å thick region of $SrTiO_3$, from a probe convergence semi-angle $\alpha = 21.3$ mrad. (a) Annular dark-field (ADF), collection angle $\alpha - 2\alpha$; (b) incoherent bright-field (BF), collection angle 0-α; (c) annular bright-field (ABF), collection angle $\frac{\alpha}{2} - \alpha$; (d) coherent bright-field, collection angle $0 - \frac{\alpha}{10}$. Experimental images are given in the left column, simulation in the right. The intensity scale is given in units of fractional intensity of the incident beam.

Table 1 compares the mean intensity and the contrast of several imaging modes to that of the corresponding simulations. For MoS_2, both the mean intensity and the contrast of the experimental images are in excellent agreement with simulations. However, for both thicknesses of $SrTiO_3$ the mean intensity of experimental ADF image is larger than that of simulation whereas the BF image mean intensity is smaller. In addition, the contrast of the experimental ADF image is notably smaller than the simulation. Since the detector is common to both the MoS_2 and $SrTiO_3$ cases, this discrepancy for $SrTiO_3$ is attributed to properties of the specimen. No obvious contamination of the MoS_2 specimen was seen during our experiments, but the $SrTiO_3$ sample had some amorphous layers on the surface, which is known to reduce the contrast of ADF images [27]. Though we have sought to minimize its severity, the slow scan rate – approximately a hundred times slower than that used for conventional imaging – causes some beam damage, which may further contribute to this effect. Slight tilt off the zone-axis can also reduce the contrast of the ADF image [28]. The distortions in the experimental ABF and cBF10 images shown in Fig. 4(c) and (d) also indicate a slight misalignment from the zone-axis.

Table 1
Mean and contrast of different imaging modes for MoS_2 and $SrTiO_3$ comparing experiment (Exp) and simulation (Sim). ADF: annular dark field; BF: bright field; ABF: annular bright field; cBF: central bright field, with outer angle $\frac{\alpha}{4}$ for MoS_2, and $\frac{\alpha}{10}$ for $SrTiO_3$.

	MoS_2				$SrTiO_3$ (35 Å)				$SrTiO_3$ (78 Å)			
	Mean		Contrast		Mean		Contrast		Mean		Contrast	
Image modes	Exp	Sim	Exp	Sim	Exp	Sim	Exp	Sim	Exp	Sim	Exp	Sim
ADF	–	–	–	–	0.11	0.06	0.28	0.71	0.12	0.08	0.17	0.34
BF	0.998	0.996	0.0035	0.0035	0.88	0.93	0.04	0.05	0.86	0.90	0.04	0.05
ABF	0.742	0.747	0.006	0.006	0.65	0.69	0.04	0.04	0.62	0.66	0.047	0.061
cBF	0.065	0.059	0.033	0.039	0.009	0.010	0.11	0.10	0.010	0.094	0.17	0.09

Simulations (not shown) indicate that even a small misalignment – e.g. 10 mrad, since for atomically fine probes on thin specimens it can be difficult to confidently achieve better alignment than this – makes the BF mean intensity smaller and the ADF mean intensity larger. It is worth mentioning that the dark reference background subtraction of the CBED patterns before synthesizing different image modes has some uncertainty, which contributes to the discrepancy of the quantification results particularly of the mean and especially for the dark field imaging modes.

4. Differential phase contrast (DPC) imaging and phase reconstruction

4.1. Quantitative DPC images

Establishing quantitative agreement between standard imaging modes and simulation as per the previous section is a good way to confirm that data from the new detector is being correctly processed. However, these imaging modes offer quantitative information on the sample, mostly at the level of confirming the general structure and perhaps counting the number of atoms (for example, that half the S atoms were missing in the MoS_2 case). By contrast, under certain conditions quantitative DPC can be used to map the full electric and magnetic field distributions within materials, from the micron scale down to atomic resolution [6,29-31,32]. Using the full 2D diffraction patterns, the first moment or center of mass for each probe position along two perpendicular directions can be calculated via [6,32,33]:

$$\langle k_x\rangle = \frac{\int k_x I(\mathbf{k}_\perp) d\mathbf{k}_\perp}{\int I(\mathbf{k}_\perp) d\mathbf{k}_\perp}; \quad \langle k_y\rangle = \frac{\int k_y I(\mathbf{k}_\perp) d\mathbf{k}_\perp}{\int I(\mathbf{k}_\perp) d\mathbf{k}_\perp}. \tag{2}$$

This center of mass can be regarded as proportional to the quantum mechanical expectation value for the transverse component of the momentum transfer [6] or, more generally, the probability current, which can be related to several specimen properties [34]. Unlike the quantitative imaging of the previous section, this imaging mode only depends on the distribution of the scattered intensity and not on its absolute scale.

In this section we synthesize DPC images for our test cases of monolayer MoS_2 and regions of 35 Å and 78 Å thick $SrTiO_3$ to explore this form of quantitative imaging. The simulated DPC images used as reference assume the same aberration parameters and Gaussian source size blurring determined from synthesized imaging modes in the previous section.

For the monolayer MoS_2 sample, Fig. 5 shows experimental and simulated DPC images, i.e. maps of the two components of the center of mass of the CBED patterns along the x and y directions defined in the bottom left corner, of the crystal structure. Both components of the experimental DPC images agree very well with the simulations in both the contrast and the DPC signal range,

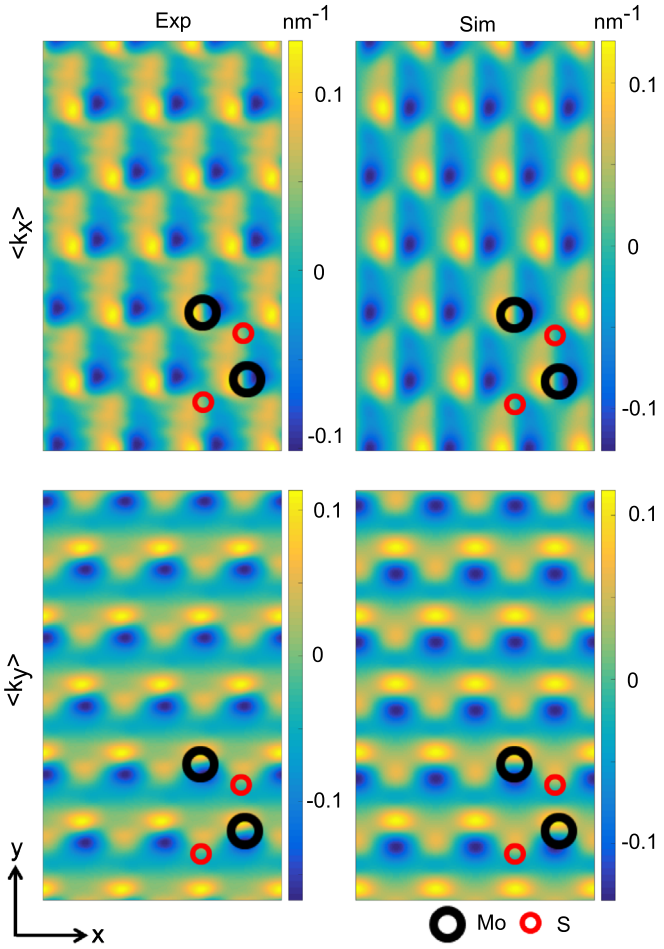

Fig. 5. Differential phase contrast (DPC) images of MoS_2. Upper row $\langle k_x\rangle$; lower row $\langle k_y\rangle$; left column experiment (Exp); right column simulation (Sim).

again showing the level of quantification which can be achieved with this 4D data.

Fig. 6 shows DPC images of $SrTiO_3$ from regions of (a) 35 Å and (b) 78 Å thickness. The experimental DPC images are largely in agreement with the simulations. However, the $\langle k_x\rangle$ image for 35 Å in Fig. 6(a) and the $\langle k_y\rangle$ image for 78 Å in Fig. 6(b) have a DPC signal range largely asymmetrical about 0 in the experimental images whereas in the simulated images they have a DPC signal range perfectly symmetric about 0. Also, in the $\langle k_x\rangle$ image for 78 Å in Fig. 6(b), both the positive and negative extrema of the experimental DPC images are smaller than those in the simulation. Asymmetry in the DPC signal range can result from inaccurate determination of the center of the central disk of the CBED

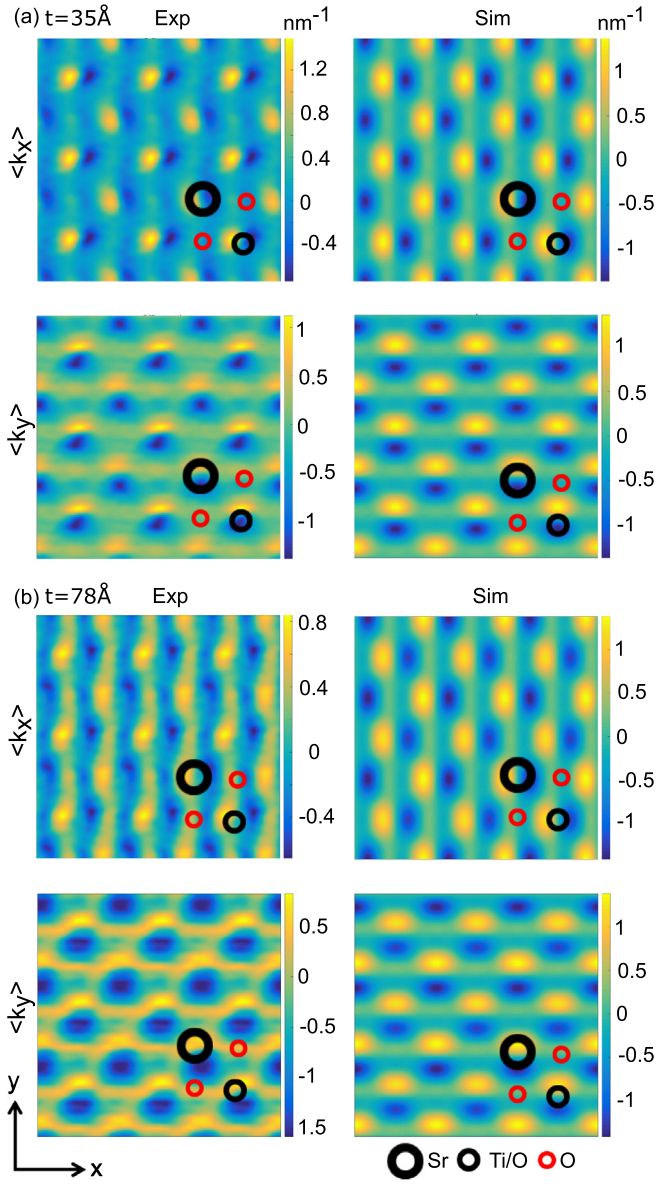

Fig. 6. Differential phase contrast (DPC) images of $SrTiO_3$ from regions of (a) 35 Å and (b) 78 Å thickness. Each figure has upper row $\langle k_x \rangle$; lower row $\langle k_y \rangle$; left column experiment (Exp); right column simulation (Sim).

patterns. However, because the edges of the bright field disk are very clear in the PACBED patterns, the uncertainty in determining the center is on the order of the sampling, less than 0.05 nm^{-1} here, which is much smaller than the discrepancies in positive and negative extrema between experimental and simulated DPC images. Misalignment of the crystal from the zone-axis can give a similar asymmetry. Simulations (not shown) indicate that our results are consistent with misalignment on the order of 10 mrad. Analysis of the PACBED patterns suggests the misalignment is unlikely to be quite that large, and consequently we believe the explanation lies in a combination of misalignment and other sources of asymmetry such as lens aberrations and residual effects of sample drift persisting through our unit-cell averaging procedure. In conventional TEM, some success has been had in identifying lens aberrations and sample tilt through image fitting [47]. However, the more time-consuming STEM image simulations make exploring the parameter space significantly more challenging, and would anyway seem to risk over-interpreting the present dataset.

4.2. Phase reconstruction from DPC images

In the phase-object approximation, the DPC images can also be used to quantitatively reconstruct the phase of the transmission function, which is proportional to the electrostatic potential of the sample [32,35]. More specifically, the reconstruction gives the convolution of the phase with the probe intensity. In this section, we seek to reconstruct the phase of the transmission function of the MoS_2 and $SrTiO_3$ samples from the experimental DPC images constructed from the 4D datasets. To do so, we must confront stability issues associated with any attempt at deconvolving the probe intensity. The diffraction-limited component of the probe intensity, which is well characterized, was deconvolved from the data. Following Ref. [32], both a high pass filter and a slightly stronger low pass filter than the bandwidth limit of twice the probe-forming aperture cut-off (2α) implied by the imaging physics was applied to suppress the low and the high frequency noise. The same filters were applied to simulations for consistency. The incoherent component of the probe intensity, which may not be very well characterized, was not deconvolved. Comparison with simulation was instead made by convolving the simulated results with the Gaussian source previously estimated. The experimental reconstructions are compared against two kinds of simulation. The first, denoted "Sim" and involving full simulation of the 4D dataset and subsequent phase reconstruction, is analogous to the comparisons made earlier: assuming the structure, multiple scattering is fully incorporated and the results constitute a quantitative consistency check. The second, denoted "Ideal" and calculated directly from the projected potential assuming an independent atom approximation (applying the same bandwidth limit and low and high pass filter as used to process the experimental data), is the result expected if the sample was a true phase object. This latter can be interpreted more directly, but constitutes an approximation which is known to break down in the presence of multiple scattering [32].

Fig. 7 shows the (a) experimental and (b) simulated reconstructions of the phase of the transmission function of MoS_2. The S and Mo atoms can be very clearly resolved. The line profile shows that the one sulfur layer assumed (instead of the two expected in stoichiometric MoS_2) gives a good match, consistent with the discussion of Fig. 2. The experimental phase is in a very good agreement with the ideal phase, excepting for a small deviation around the Mo position which is attributed to discrepancies at the high scattering angles due to thermal scattering. Note that the "Sim" and "Ideal" results are very similar because channeling effects are negligible in monolayer MoS_2. To show the effects of the distortion correction and averaging procedure used, Fig. 7(d) and (e) show the raw image (cBF4) and DPC reconstructed phase from the MoS_2 sample. In Fig. 7(d), the Mo atoms are clearly visible despite the monolayer nature of the specimen. However, the low SNR prevents unambiguous identification of the S atoms. The sulfur atoms are clearer in the reconstructed phase in Fig. 7(e). However, the phase at different S atom sites varies widely (two different S atom positions are indicated by the arrows in Fig. 7 (d) and (e)), illustrating that some sulfur atoms are knocked out during the imaging acquisition. At present, the raw phase image is too noisy to be used to quantify the number of sulfur atoms reliably, though lower beam voltage and higher dose might reduce the radiation damage while improving the SNR sufficiently to allow processing of the raw phase image directly.

Fig. 8 shows the reconstructed phase of the transmission function of the $SrTiO_3$ sample for the (a)–(c) 35 Å and (d)–(f) 78 Å thick regions. Oxygen columns can be clearly seen in the reconstructed experimental phase from both these thicknesses. While the experimental profiles in Fig. 8(c) and (f) are qualitatively similar to the simulations, the experimental reconstructions have

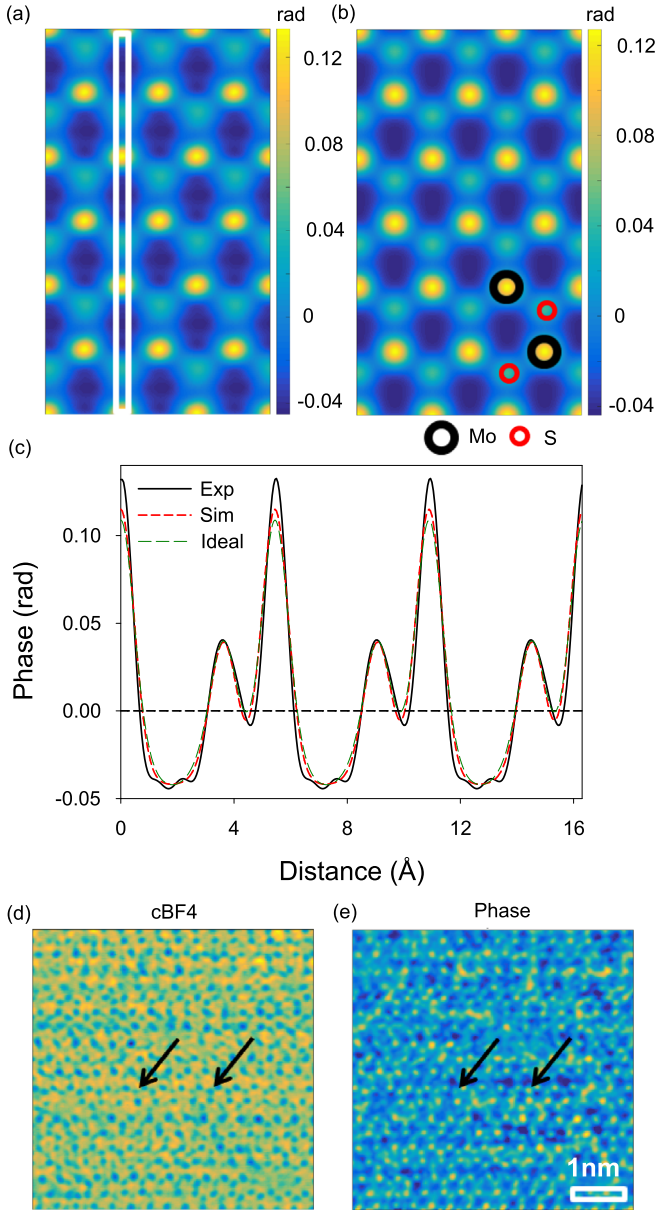

Fig. 7. (a) Experimental and (b) simulated (assuming defocus $f = -50$ Å and source size 0.45 Å) reconstructions of the phase of the transmission function of MoS_2. Note that the simulated phase used only one sulfur layer, as discussed in reference to Fig. 2. (c) Profiles of the phase reconstructions along white rectangular region in (a) comparing experiment (Exp), 4D data simulation (Sim), and a phase calculated directly from the projected potential (Ideal). (d) Experimental raw cBF4 image (collection angle $0 - \frac{\alpha}{4}$) and (e) DPC reconstructed phase of MoS_2. Arrows in (d) and (e) indicate two sulfur atom positions.

smaller phase range than the simulations with the discrepancy being larger at the larger thickness. Note that this is different to the reduction in reconstructed phase range due to channeling discussed in Ref. [32] because the "Sim" profiles include the channeling effect. Rather, uncertainties in probe characterization (effective source size, defocus and uncompensated/unknown probe aberrations and/or drift of the corrector over time), noise, specimen misalignment – directly evident in the slight asymmetry in Fig. 8(a) and (d) – and amorphous surface layers may all contribute to this effect.

A brief comment is warranted on comparing the reconstructed

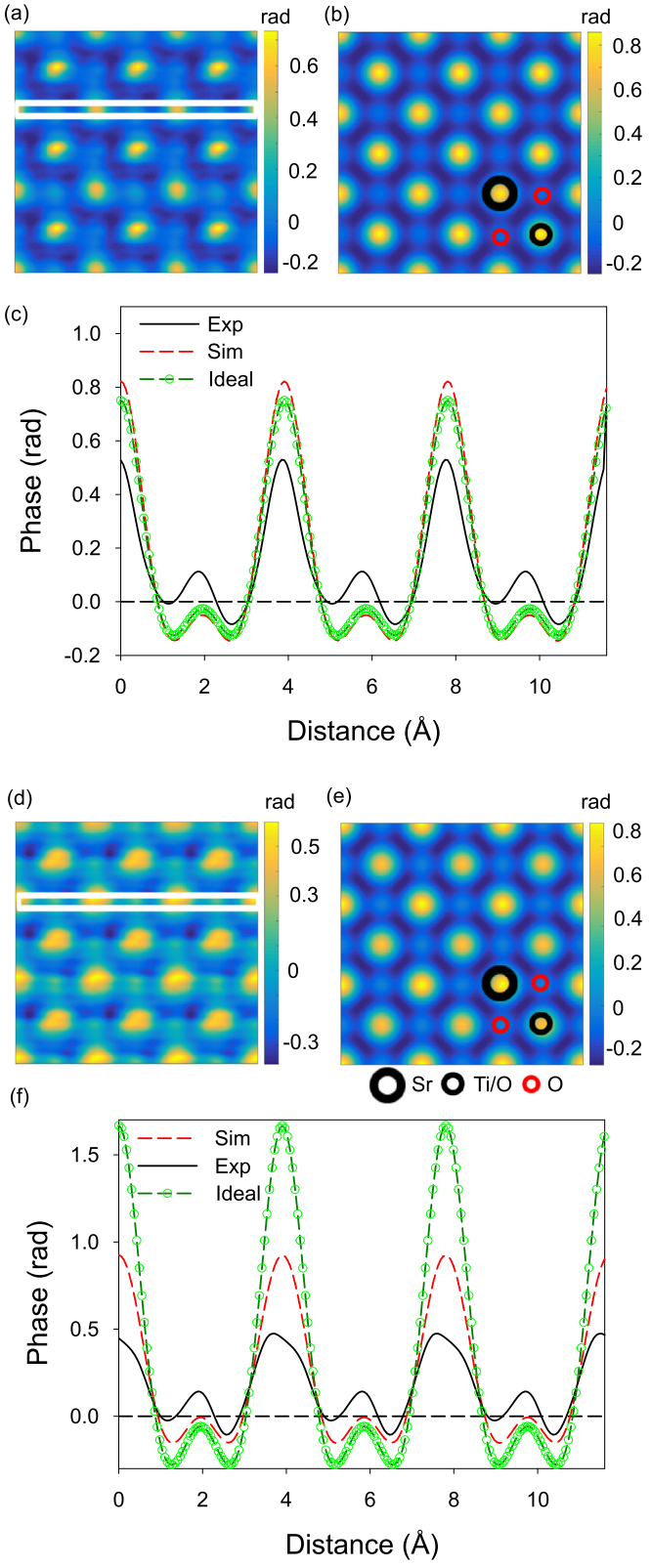

Fig. 8. (a) Experimental and (b) simulated (assuming defocus $f = -30$ Å and source size 0.50 Å) reconstructions of the phase of the transmission function of $SrTiO_3$ at a thickness of 35 Å. (c) Profiles of the phase reconstructions along white rectangular regions in (a) comparing experiment (Exp), 4D data simulation (Sim), and a phase calculated directly from the projected potential (Ideal). (d–f) As per (a–c) but for a thickness of 78 Å and assuming defocus $f = -20$ Å in the simulation.

phase from simulated DPC images with the ideal phase-object phase. The small difference between "Sim" and "Ideal" simulations in Fig. 8(c), which is most pronounced on the strongly scattering Sr columns, shows that channeling effects are beginning to manifest for a thickness of 35 Å in $SrTiO_3$. That the phase range is larger in the "Sim" than the "Ideal" profiles on the Sr columns in Fig. 8(c) appears to be a consequence of the defocus being appreciably different from its optimal location of the midplane [32]. For the thicker 78 Å case in Fig. 8(f), the "Ideal" phase, which scales linearly with thickness, is much larger than both the "Sim" and "Exp" phases and it is thus clear that the phase-object approximation has broken down for the 78 Å thick $SrTiO_3$ sample.

As presented above, DPC offers a simple and fast constructive algorithm for phase reconstruction, but it is not the only approach to phase reconstruction from 4D data, the most established alternative in the STEM geometry perhaps being ptychography. Constructive algorithms exist for ptychography from weakly scattering objects, which have been shown to constitute an optimally electron-efficient processing of 4D data [7,9]. For strong phase objects, ptychography tends to involve iterative approaches [36–38]. In principle, one of the strengths of ptychography is super-resolution: iterative ptychography is not bandwidth limited by the probe-forming lens. However, in practice the attainable outer scattering angle of the diffraction pattern is limited by either SNR or detector size. As the next section will show, for our current datasets the scattering angles higher than the bandwidth limit of 2α used in the DPC phase reconstruction are dominated by noise – iterative ptychography would not be expected to yield any further information.

5. Statistical analysis, SNR enhancement and data size reduction of 4D datasets

The full scattering distribution in the set of CBED patterns in the 4D dataset is often presented as being rich in information, especially in comparison to individual, conventional imaging modes as synthesized in previous sections. However, while fine features are present within the simulated CBED patterns, the sensitivity, SNR and dynamic range of the camera mean that their reliable detection is not guaranteed. Focusing particularly on the SNR limit of such datasets, this section presents guidelines about the extent and sampling of the CBED patterns beyond which information becomes lost in the noise. Such conclusions can then be fed back into experimental design and execution, facilitating data acquisition by seeking to record the smallest amount of data which still contains the majority of the information content.

5.1. Practical constraints on maximum useful scattering angle

One simple metric for the information content in the 4D data is the amplitude of the variation of the CBED patterns both along radial and azimuthal scattering angles. The information in the atomically resolved CBED patterns is only accessible if it is greater than the SNR prevailing under the experimental conditions used. To explore this issue, we present a statistical analysis on CBED patterns from $SrTiO_3$ assuming $\alpha = 21.3$ mrad and with the probe situated on the Sr column, since this heavy column is expected to give the maximum scattering to high angles. We stress at the outset that in discussing SNR in reference to the simulated CBED patterns we are considering the fundamental statistical limit (i.e., shot noise) due to the finite dose, which applies even to the ideal detecting system. In practice, device-dependent sources of noise, such as readout noise, degrade the SNR still further.

The left column in Fig. 9 shows simulated CBED patterns for (a) 35 Å and (b) 200 Å thick samples, for both a coherent probe and a probe incorporating spatial incoherence, and (c) a comparison between experiment and simulation for a nominal thickness of 78 Å. (Source size broadening is incorporated into the simulated CBED patterns following Ref. [39].) As expected, the contrast and fine structure of the CBED patterns tend to increase with specimen thickness. However, the source size broadening is seen to dramatically diminish the contrast and fine features in the CBED pattern compared with the coherent probe case. Note too that the experimental pattern in Fig. 9(c) does not quite show the four-fold symmetry expected of the Sr column, suggesting a slight mistilt and some residual drift and/or bias in the procedure used to produce the averaged dataset.

The middle column in Fig. 9 shows the intensity variation as a function of azimuthal angle for several selected radial scattering angles, assuming a small intensity averaging area with a radial width of 0.63 mrad. For the very thin sample, 35 Å in Fig. 9(a), the intensity variation in the azimuthal direction is small, especially at large radial scattering angles. For the thicker sample, 200 Å in Fig. 9(b), the variation is much larger, even at large radial scattering angles, meaning that much more information would be lost if an annular detector were used instead. Despite the asymmetry in the experimental pattern in Fig. 9(c), the variation across azimuthal angle is similar in both the experiment and simulation, except for the highest radial scattering angle, 42.7 mrad, in which the experimental variation is starting to become lost to the noise level. There is some difference in quantitative scale, consistent with the discrepancies in dark field contrast noted in the discussion of Fig. 4 and Table 1 which we attribute to amorphous surface layers and specimen mistilt.

The right column in Fig. 9 shows the mean and standard deviation of the azimuthal intensity variation as a function of the radial scattering angle. The mean azimuthal intensity is seen to typically be at least one and often two orders of magnitude smaller by a scattering angle of 2α than it is within the bright field region, with spatial incoherence enhancing this effect. Consistent with the appearance of the CBED patterns, the inclusion of spatial incoherence also reduces the standard deviation in the azimuthal intensity by almost one order of magnitude in the $t = 35$ Å case. Again, despite the asymmetry in the experimental pattern in Fig. 9(c), the mean and standard deviation curves are overall in good qualitative and broad quantitative agreement between experiment and simulation.

Though very fine features are present within the simulated CBED patterns, the SNR and dynamic range of the camera mean that it is not guaranteed that we could observe them. Thinner and/or more weakly scattering objects give a stronger transmitted beam, weaker diffracted beams and smaller pattern contrast, requiring a larger SNR and camera dynamic range to observe the fine structures in the CBED patterns. Even for thick and/or strongly scattering objects, like our 200 Å-thick, Sr column example, both the mean and the standard deviation of the azimuthal intensity variation is an order of magnitude smaller at high radial scattering angles ($> 2\alpha$) than it is in the low scattering angle region. These considerations place an outer limit on the radial scattering angle at which CBED intensity variation is detectable with the current detector technology. Beyond this region there is no clear merit to using a pixel detector: traditional ADF detectors could be used to obtain the integrated signal from this region, leaving the pixel detector to be used either at finer sampling or with fewer pixels within the lower scattering angle region.

Simulation together with the current experimental parameters can be used to make an estimate of the SNR level due to shot noise as follows. The beam current used, 65 pA, corresponds to $4 \times 10^8 e^-$ per second. Combined with the acquisition speed of 400 frames per second, this corresponds to $10^6 e^-$ per frame. Therefore, any pixel with fractional intensity of 10^{-6} is expected to record just one

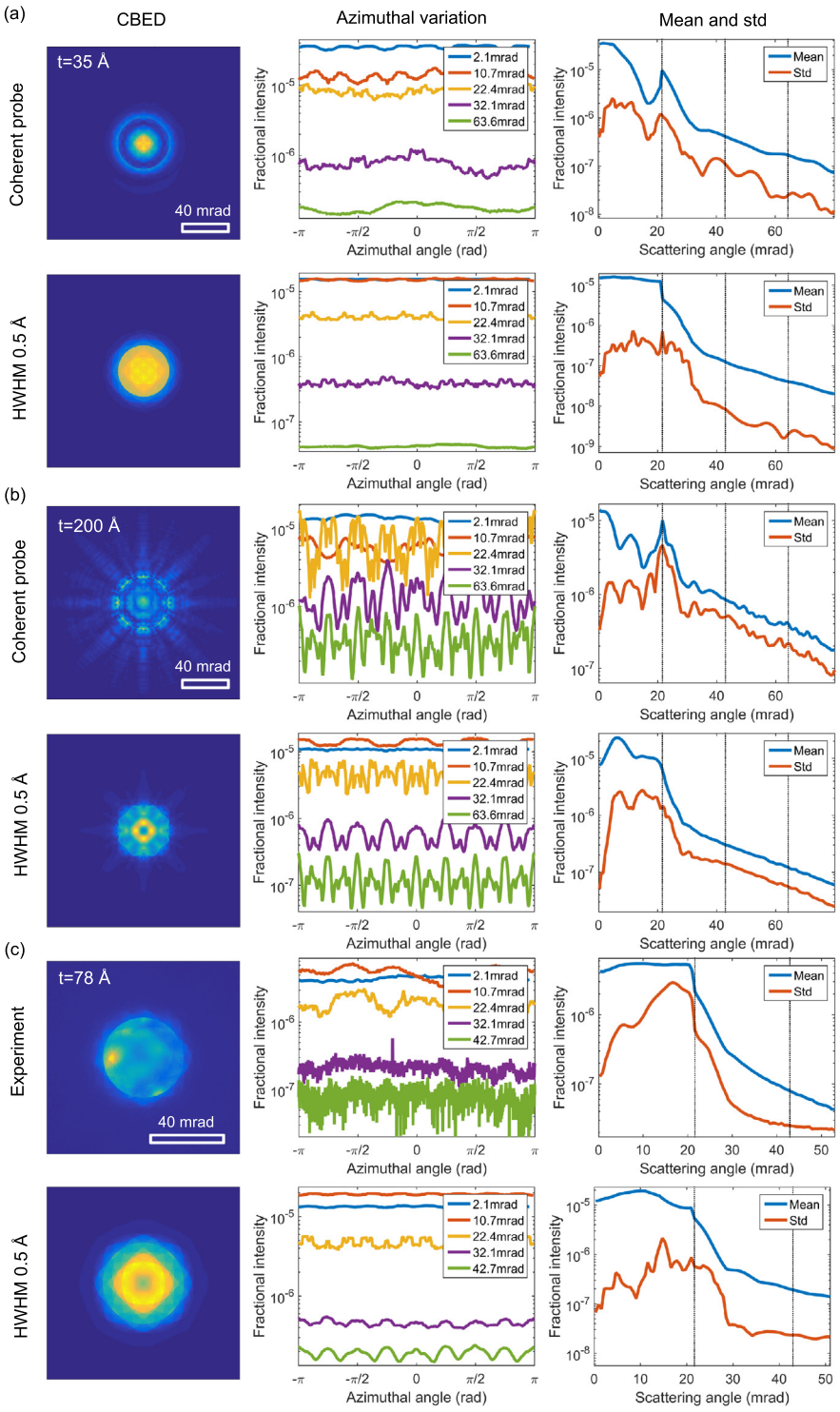

Fig. 9. Statistical analysis of CBED patterns from the $SrTiO_3$ sample when the probe is on a Sr column for thicknesses of (a) 35 Å and (b) 200 Å in simulation, and (c) 78 Å comparing experiment (after the unit cell averaging process) with simulation. Left column, diffraction pattern; middle column, intensity variation as a function azimuthal angle for five select radial scattering angles; right column, mean and standard deviation per pixel as a function of radial scattering angle (averaged over an annular ring of width 0.63 mrad).

electron, which, assuming Poisson statistics, corresponds to a SNR of 1. From Fig. 9(a) and (b) we find that, for the CBED sampling considered, the fractional intensity falls below 10^{-6} beyond about 1.5α. The experimental pattern in Fig. 9(c) has been averaged over about 50 equivalent sites, giving $5 \times 10^7 e^-$ per frame, improving the SNR to above 3 out to about 2α. Note that Fig. 9 shows the point-to-point variation in intensity, the "Std" of the right column, to be consistently smaller than the mean intensity, meaning that the SNR is lower for any information contained in the intensity variation.

A good SNR for reliable estimation of the CBED pattern (a notably more stringent requirement than the confidence in the number of electrons detected) usually requires the number of counts per pixel to be at least ten to one hundred electrons. The total dose can be varied in three ways, which can be used in conjunction: dwell time, current and repeat averaging. Increasing

the dwell time is problematic as it would worsen specimen drift problems which are already appreciable in the current dataset. Since a high brightness gun can give up to 1 nA [40], increasing the beam current is certainly possible (it would likely increase the beam damage, but this could be ameliorated by working at lower beam voltages). Fast acquisition over large sample regions and subsequent averaging during image analysis – the approach used here – is also possible, but requires either a periodic sample or else multiple scans over the same region. The number of counts per pixel can also be increased by increasing the pixel size, either through choice of camera length or by binning in post-processing. Whether such an approach would eliminate the very fine feature variation we are striving to detect is explored further in the next section.

In summary, three times the convergence angle could be considered a conservative outer limit with detectable pixel-by-pixel variations based on existing or near-future operating conditions and in specimens similar to $SrTiO_3$ at moderate thicknesses. It should be emphasized that the analysis above is the fundamental limit based on the statistics of detecting quantum particles. Current systems are likely to have lower SNR due to their detection quantum efficiency [18] and the readout and Landau noise, though the latter may be avoided or significantly reduced by using a counting mode [17] or a thicker detector design [41]. Note too that the outer angle limit determined from the observable intensity variation also depends on the scattering strength of the objects (elements, probe position, orientation, etc.), camera properties and convergence angle of the probe.

5.2. Sampling of the diffraction pattern

Currently, pixel detectors are designed principally as recording devices for TEM images, where more pixels is usually seen as better. However, for the present experiment the pixel width in the CBED patterns is only 0.1 mrad and we might rather ask whether such fine sampling was really necessary. There are many benefits if fewer pixels of the 2D camera are required. Fewer pixels within one diffraction pattern can increase the acquisition speed, reduce the data storage requirements and facilitate rapid analysis. In addition, requiring fewer pixels can relax the restriction on the physical size of each pixel/sensor, reducing the commercial expense and increasing the SNR [42]. Yang et al. [9] have explored the minimum number of pixels needed to maximize peak SNR for ptychography. We explore the number of pixels needed in terms of edge detection and preservation of information content in the CBED patterns.

Beginning with highly sampled CBED patterns – the radius of the bright field disk being more than 100 pixels – as a reference, we generated a series of down-sampled images by successive binning over 2×2 pixel blocks. The CBED patterns for different sampling were compared against the reference by evaluating the L^2-norm metric between the reference and the binned images up-sampled by bicubic interpolation back to the original sampling. This assesses the extent to which information content in the fine features of the original patterns is preserved in the binned images (as information lost to binning is not expected to be retrievable by bicubic interpolation, which contains no physical insight about the structure of diffraction patterns). The larger the L^2-norm value obtained, the larger the difference between the reference and the down-sampled pattern, which means more features have been lost to the down-sampling process.

Fig. 10(a) shows the maximum value of the L^2-norm across all probe positions in the scan for different degrees of binning, given in terms of the pixel radius of the bright field disk. Results are shown for a few different thicknesses of the $SrTiO_3$ sample. All plots include spatial incoherence with a Gaussian effective source

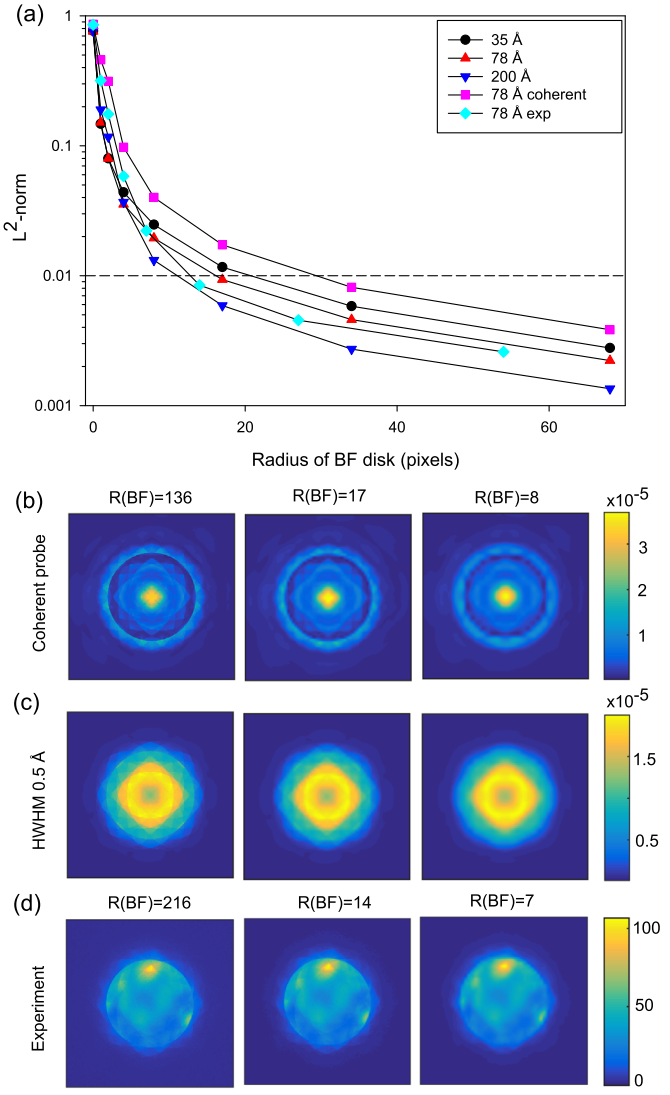

Fig. 10. Sampling analysis of CBED patterns for $SrTiO_3$. (a) Maximum value of the L^2-norm between the reference and the down-sampled CBED patterns over all probe positions in the scan in terms of the pixel radius of the bright field disk (R (BF)). Simulated results are shown for a few different thicknesses of the $SrTiO_3$ sample. All plots include spatial incoherence with a Gaussian effective source of 0.5 Å HWHM, except for that plot labeled "coherent". Experimental data, labeled "exp", is also given for the 78 Å thick case. (b)–(d) Different sampling of one diffraction pattern when the probe is on the Sr column in a $SrTiO_3$ sample of thickness 78 Å for (b) the coherent probe, (c) assuming a Gaussian source HWHM 0.5 Å and (d) experiment.

of 0.5 Å HWHM, except for that labeled "coherent" and the experimental data (labeled "exp"). It is seen that a bright field disk radius of only about 15 pixels suffices to give an L^2 value below a threshold of 0.01. Fig. 10 also shows the effect of binning on one CBED pattern for (b) a coherent probe, (c) a Gaussian source with HWHM = 0.5 Å, and for (d) experimental data. When the radius of the bright field disk is about 8 pixels, the fringes within the pattern are mostly smeared out, giving a visual sense of the changes that Fig. 10(a) shows through the simple L^2-norm metric. While CBED patterns are not formally bandwidth limited by the image formation physics, a variant on this approach is to identify the minimum (Nyquist) sampling corresponding to a pragmatic bandwidth limit based on where the intensity of the Fourier transform of the ideal CBED patterns drops below the noise level

of these images.[1] Because setting a lower L^2 norm difference corresponds to keeping more fine features of the CBED patterns and these correspond to high frequency information, these two approaches give very similar results for the ideal data shown here. The Fourier approach would, however, more constructively allow for incorporating a particular experimental noise level.

If, as per the previous section, we only sought to acquire CBED patterns out to a radial scattering angle of three times the bright field disk radius, we would only need a camera with about 90×90 pixels (corresponding to about 40×40 binning applied to a $4\,\mathrm{K} \times 4\,\mathrm{K}$ camera like the K2-IS used here) to reach the threshold of $L^2 = 0.01$. If the effective source size is reduced, approaching the coherent case, finer features become evident in the CBED patterns and more pixels are required in the bright field disk to obtain the same L^2-norm fidelity. The threshold of $L^2 = 0.01$ is somewhat arbitrary, but corresponds to a maximum change from down-sampling of less than 1% in the synthesized incoherent or coherent bright field imaging modes and middle angle range (inner collection angle larger than about 1.5α) annular dark field images. (The difference is larger, up to 20%, for the low angle annular dark field image with inner collection angle of α, in part because the binning procedure obscures the location of the edge of the bright field disk and redistributes some intensity from the bright field into the dark field region.) In summary, a 128×128 pixel camera, such as that used in Ref. [41], would suffice for synthesizing most standard imaging modes considered in Section 3 to a high degree of accuracy.

5.3. Principal component analysis (PCA) and data reduction

4D datasets are touted as a rich source of information. However, large datasets also present challenges, not only in acquisition, storage and manipulation, but also in identifying features of interest when little is known *a priori* about what they may be. The previous section showed a significant degree of binning to be possible without much loss of information, implying that nearby pixels contain similar, and thus potentially redundant, structural information. PCA is an established technique for identifying statistically significant information [43,44], for seeking the minimum number of orthogonal modes needed to describe the nontrivial structure in multi-dimensional datasets, and conversely for identifying and getting rid of redundant modes to reduce both noise and the data size. In this section, we focus on using PCA to reduce the size of the huge 4D dataset, and by implication as a crude metric of the information content.

PCA can be applied to multidimensional data in various ways. In principle, STEM images can be formed for each single pixel in the CBED pattern. Therefore, we consider the STEM image formed for each pixel in a CBED pattern as the observation and the pixel location in the CBED pattern as the variable. Prior to PCA analysis, the STEM images in vector form were set to have zero mean and unity standard deviation. This normalization treats structure in the bright and dark field region more equally than their true absolute intensity would imply, thus favouring information in the form of STEM image structure over STEM image intensity. We first apply this analysis to simulated 4D datasets for $SrTiO_3$ for both 35 Å and 200 Å thick samples. The CBED patterns were 512×512 pixels and the STEM scan 20×20 pixels, and 80 phonon configurations were used during the simulations to reduce the numerical noise. The PCA procedure then decomposes the 4D dataset $\mathcal{I}(\mathbf{k}_\perp, \mathbf{R})$ into the form

$$\mathcal{I}(\mathbf{k}_\perp, \mathbf{R}) = \sum_{i=1}^{N} D_i(\mathbf{k}_\perp) I_i(\mathbf{R}), \tag{3}$$

where we can think of $D_i(\mathbf{k}_\perp)$ as (orthogonal) synthetic detector weighting functions and the $I_i(\mathbf{R})$ as the corresponding STEM images. Since the particular form of the matrices $D_i(\mathbf{k}_\perp)$ and $I_i(\mathbf{R})$ obtained depends on the scattering in the specimen, the probe function, the noise transfer function and the detector's point spread function, it is difficult to associate a particular physical meaning with the individual matrices. However, such a decomposition is always possible for N equal to the number of pixels in the STEM image (technically one less than this, given our choice of zeroing the mean). The PCA decomposition can rank, by eigenvalue magnitude, the terms in Eq. (3) in order of decreasing contribution to the significant variation in the 4D dataset. If the significant variation can be accounted for by a small number of basis functions, the dataset is said to be reducible. If so, retaining just this small number of basis functions and the corresponding coefficients suffices to enable any imaging mode or indeed the full dataset to be reconstructed to a good level of accuracy. This has the practical advantage of reducing the data size. It also gives a sense of how much information is truly present in the original dataset.

Fig. 11(a) and (d) show the sorted eigenvalues versus the component number, a so-called scree plot, for simulated 4D datasets of $SrTiO_3$ for the two thicknesses. In significantly redundant datasets, such scree plots typically have an “elbow”, an identifiable turning point beyond which the reduction in eigenvalue with increasing component number becomes very flat [45]. Components before the elbow are interpreted as being significant whilst those beyond it are interpreted as being dominated by noise. With this in mind, very different behavior is seen between the coherent probe case and that with spatial incoherence (labeled “HWHM 0.5 Å”). The case with spatial incoherence shows a dramatic initial reduction in eigenvalue magnitude until around 80–90 components, after which it becomes very flat. By contrast, for the coherent probe the decrease is continuous, suggesting no clear transition to structureless noise and perhaps therefore that nontrivial information persists into the high order components. This strongly reinforces the impression from the previous sub-sections that spatial incoherence, by smoothing away some fine features, appreciably reduces the information content present in the 4D dataset. Pragmatically, though, the eigenvalues in the coherent case do get successively smaller, and for the purposes of data reduction it may be that keeping only the first 100 or so components allows for a tolerably good estimate of the raw dataset. To cast this in more intuitive terms and to check whether the raw dataset can be well reproduced using a limited number of components, Fig. 11 (b), (c), (e) and (f) show the difference between the full 4D dataset and the reconstruction using a truncated version of Eq. (3), for the CBED pattern for the Sr column, and BF, ADF and DPC STEM images.

For the coherent probe, Fig. 11(b) and (e), truncating to 30 components shows residual structure in the difference CBED patterns at the 10% level for the thin sample (35 Å, Fig. 11(b)) and 50% level for the thicker sample (200 Å, Fig. 11(e)). Truncating to 80 or 90 components, the residual difference in the CBED pattern drops to around 1% for the thin sample and around 3% for the thicker sample. Structure is still visible in the difference CBED pattern, suggesting that the rest of the PCA components may contain nontrivial information (though there is reason to think that the highest order modes contain “noise” due to the finite number of frozen phonon configurations used). However, this fine and oscillatory structure will largely average out in most standard imaging modes. For the BF and ADF images, the residual variations after 80 to 90 components are all smaller than 1% of the original image, even for the thicker sample. For the DPC images, the differences

[1] We are grateful to one of the reviewers for this observation.

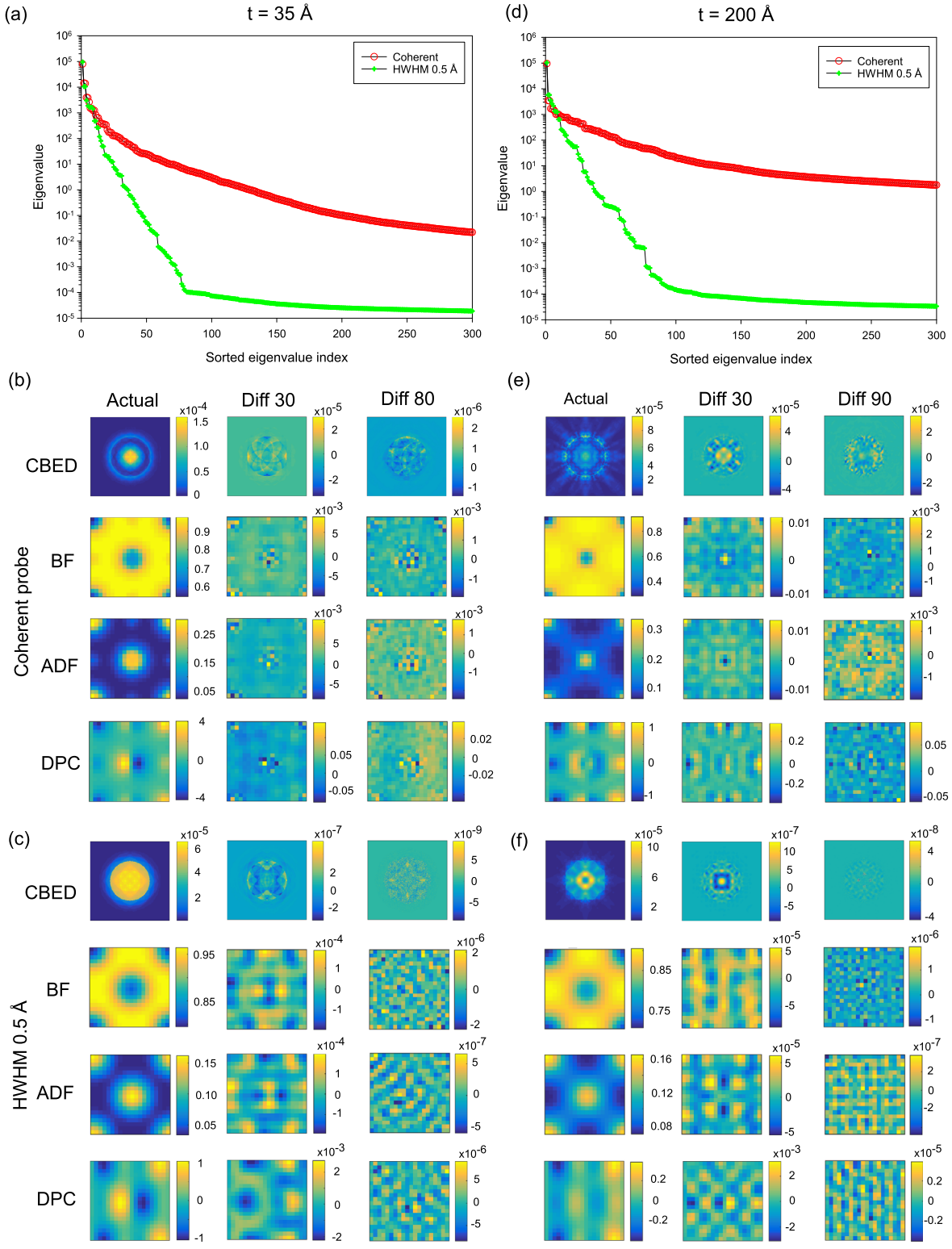

Fig. 11. PCA analysis on two simulated datasets from $SrTiO_3$: (a)–(c) thickness 35 Å; (d)–(f) thickness 200 Å. (a) and (d) eigenvalues of PCA analysis; (b) and (e) CBED pattern and different synthesized STEM imaging modes for a coherent probe; (c) and (f) CBED pattern and different STEM imaging modes for a Gaussian source with 0.5 Å HWHM. In addition to the ("actual") images, the difference between the actual image and those reconstructed using the first 30 and 80 (90) PCA components are also shown. The DPC images show $\langle k_x \rangle$ only.

are slightly larger, about 1% for thinner sample and 5% for thicker sample.

Consistent with the behavior of the scree plots in Fig. 11(a) and (d), far fewer components are required for high accuracy reconstruction for the case of a Gaussian incoherent effective source of 0.5 Å HWHM in Fig. 11(c) and (f). Truncating to 30 components shows residual structure in the difference for CBED two orders of smaller than that in the original CBED. Truncating to around 80–90 components, the reconstruction is indistinguishable from the original CBED pattern. For the synthesized BF, ADF and DPC STEM

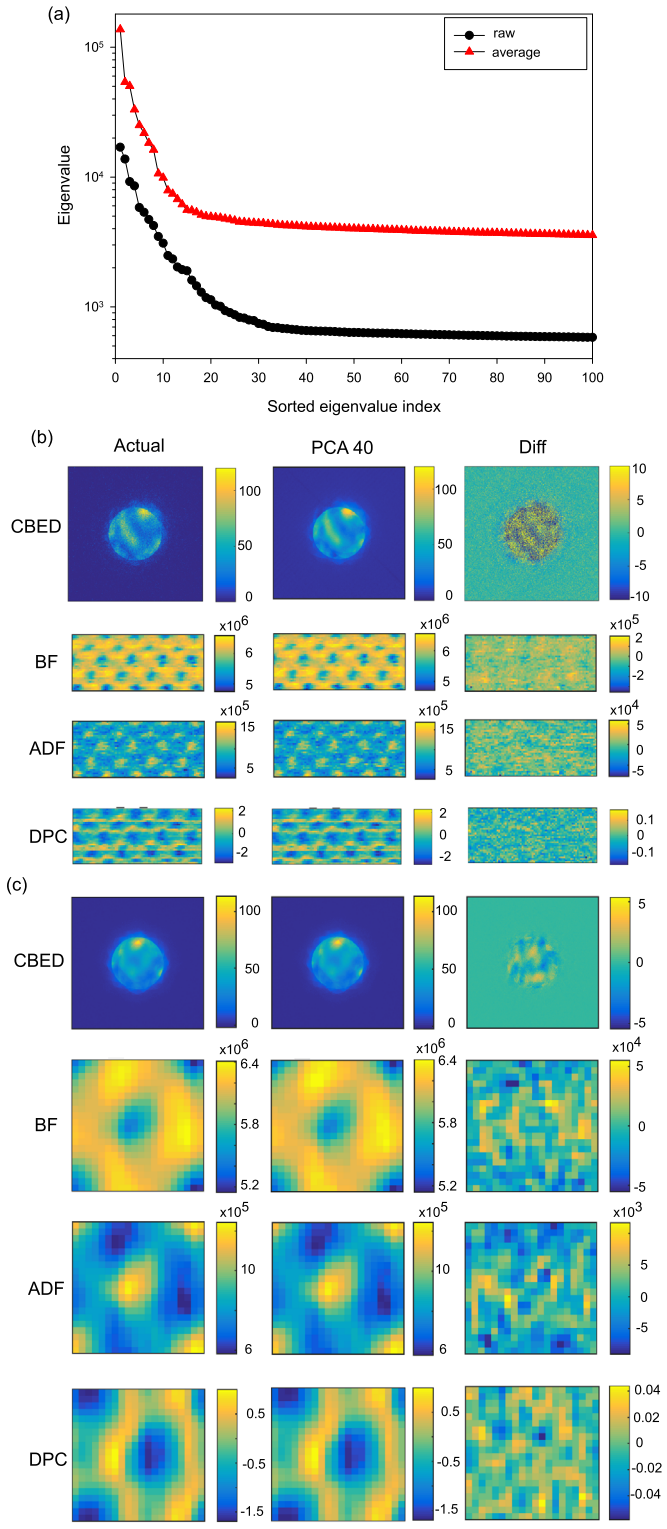

Fig. 12. PCA analysis on the experimental 4D dataset from a 78 Å thick $SrTiO_3$ specimen. (a) The eigenvalues from PCA analysis from both the raw data from a large scanning area ("raw") and the one-unit-cell dataset resulting from the repeat unit averaging ("average"). For the CBED pattern on the Sr column and for synthesized STEM imaging modes, the actual image, that reconstructed using the first 80 components and the difference between these are shown for (b) the raw data from a large scanning area and (c) the one-unit-cell dataset resulting from repeat unit averaging. The DPC images show $\langle k_x \rangle$ only.

images, truncating to 30 components gives a residual difference much smaller than 1%, adequate even for quantitative applications, and using 80–90 components gives residual variation four to five orders of magnitude smaller than the original signals.

Different imaging modes such as HAADF, BF and ABF usually contain different aspects of the structural information of the specimen. The first few detector weighting functions $D_i(\mathbf{k}_\perp)$ (not shown) of Eq. (3) are reminiscent of these standard modes, to the extent that they either have a high degree of rotational symmetry (and so look like combinations of BF, ABF and ADF detectors) or directionality (and so look like DPC detector weighting functions). Beyond these basic symmetries, though, we have found sufficient variation in the detail of the high order modes between different materials and between the same material at different thicknesses that we are reluctant to assign physical meaning to individual modes. However, even without seeking a particular physical interpretation for the individual components, it is interesting to know how many modes are required to keep most of the structural information. Our results show that PCA can be used to reduce the dataset dramatically. Keeping only the first 30 components, the dataset size is reduced by about 92% for this one unit cell $SrTiO_3$ simulated dataset. Keeping about the first one hundred components gives a smaller but still appreciable size reduction of 75%. Furthermore, assuming a periodic specimen, larger datasets containing more scanning positions would not increase the required number of PCA components significantly. Thus a data size reduction of one hundred times would be readily achievable if the dataset contains multiple unit cells within the scanning area.

We demonstrate this by applying PCA to a real experimental 4D dataset, both in raw form (2×4 unit cells) from a large scanning area and in one-unit-cell form resulting from the repeat unit averaging following the prescription in Section 2. As judged from the scree plot in Fig. 12(a), about 20 components (total 399) for the averaged dataset and 30 components (total 2540) for the raw dataset account for the most significant variation. Choosing the first 40 PCA components, as shown in Fig. 12(b) and (c), is seen to account for the overwhelming majority of the variation. This is especially evident in the difference images in the right column, where the only features visible appear to be random noise. The raw CBED, labeled as "Actual", in Fig. 12(b) is very noisy and it is hard to see the edges of diffraction disks. However, using 40 PCA components, the reconstructed CBED is much less noisy and the edge of the diffraction disks can be located explicitly: PCA can improve the SNR significantly. The residual intensities of the BF, ADF and DPC images, right column in Fig. 12(b), all contain mostly noise without significant structure features. For the averaged dataset in Fig. 12(c), there is likewise no significant structural variation in the residual image. Furthermore, variation of the residual image is less than 1% in the BF and ADF images and only a few percent in the DPC image.

In summary, keeping only the first 40 PCA components in our datasets maintains almost all structural information while reducing the dataset by about two orders in magnitude: the raw dataset used here (2×4 unit cells) can be reduced from 10 GBs to about 100 MBs. The degree of data reduction possible by PCA is a consequence of redundancy in the huge dataset and serves as another metric of information content. In the present case, the information content has proven to be notably smaller than the raw data size would suggest, primarily as a consequence of information lost to spatial incoherence and low SNR. This enables a high degree of data reduction, with the increased ease of data transfer and analysis being a consolation of sorts. Conversely, when more information is contained in the dataset, perhaps because the coherence is higher or the sample structure is more complex,[2] the

[2] Very recently, Jesse et al. [46] applied PCA to an experimental 4D dataset from a complex interfacial structure in $BiFeO_3$ and still achieved data reduction of more than 90%.

reduced degree of compression is the price of the additional information.

6. Conclusion

Multiple imaging modes synthesized from 4D diffractive imaging datasets – including DPC imaging and the associated reconstructed phase – show good quantitative absolute intensity scale agreement between experiment and simulation, though the bright field and near dark field regions show a degree of sensitivity to amorphous surface layers and specimen mistilt. Through exploring the intensity variation in the CBED patterns and the SNR limits for the present and fairly standard imaging conditions, we see scant benefit to collecting CBED patterns to scattering angles beyond about three times the bright field disk radius or at sampling greatly exceeding 128×128 pixels. Through PCA analysis, the present datasets could be reduced in size by around two orders of magnitude, greatly facilitating data transfer and preliminary analysis. A major contributing factor to this is the finite source size condition, which was shown to smooth fine features in the CBED patterns. It may be that reducing spatial incoherence would enable more information to be preserved in the 4D datasets, though a meaningful metric for this remains to be found.

Acknowledgments

The authors wish to thank Drs N.R. Lugg and P.R. Miller for helpful discussions. This research was supported under the Australian Research Council's Discovery Projects funding scheme (Projects DP110102228 and DP140102538) and its DECRA funding scheme (Project DE130100739). Work at the Molecular Foundry was supported by the Office of Science, Office of Basic Energy Sciences, Office of the U.S. Department of Energy under Contract No. DE-AC02-05CH11231. The Monash Centre for Electron Microscopy is acknowledged for providing facilities for sample preparation, initial microscopy and data analysis.

References

[1] J.M. Rodenburg, B.C. McCallum, P.D. Nellist, Experimental tests on double-resolution coherent imaging via STEM, Ultramicroscopy 48 (1993) 304–314.
[2] N.J. Zaluzec, Quantitative measurements of magnetic vortices using position resolved diffraction in Lorentz STEM, Microsc. Microanal. 8 (2002) 376–377.
[3] J. Tao, D. Niebieskikwiat, M. Varela, W. Luo, M.A. Schofield, Y. Zhu, M. B. Salamon, J.-M. Zuo, S.T. Pantelides, S.J. Pennycook, Direct imaging of nanoscale phase separation in $La_{0.55}Ca_{0.45}MnO_3$: relationship to colossal magnetoresistance, Phys. Rev. Lett. 103 (2009) 097202.
[4] K. Kimoto, K. Ishizuka, Spatially resolved diffractometry with atomic-column resolution, Ultramicroscopy 111 (2011) 1111–1116.
[5] C. Ophus, P. Ercius, M. Sarahan, C. Czarnik, J. Ciston, Recording and using 4D-STEM datasets in materials science, Microsc. Microanal. 20 (2014) 62–63.
[6] K. Müller, F.F. Krause, A. Béché, M. Schowalter, V. Galioit, S. Löffler, J. Verbeeck, J. Zweck, P. Schattschneider, A. Rosenauer, Atomic electric fields revealed by a quantum mechanical approach to electron picodiffraction, Nat. Commun. 5 (2014) 5653.
[7] T.J. Pennycook, A.R. Lupini, H. Yang, M.F. Murfitt, L. Jones, P.D. Nellist, Efficient phase contrast imaging in STEM using a pixelated detector. Part I: experimental demonstration at atomic resolution, Ultramicroscopy 151 (2015) 160–167.
[8] H. Yang, L. Jones, H. Ryll, M. Simson, H. Soltau, Y. Kondo, R. Sagawa, H. Banba, I. MacLaren, P. D. Nellist, 4D STEM: high efficiency phase contrast imaging using a fast pixelated detector, J. Phys.: Confer. Ser. 644 (2015) 012032.
[9] H. Yang, T.J. Pennycook, P.D. Nellist, Efficient phase contrast imaging in STEM using a pixelated detector. Part II: optimisation of imaging conditions, Ultramicroscopy 151 (2015) 232–239.
[10] P. Ercius, Open NCEM (2015). URL ⟨https://bitbucket.org/ercius/openncem/src/255748743f26?at=master⟩.
[11] J.M. LeBeau, S.D. Findlay, L.J. Allen, S. Stemmer, Position averaged convergent beam electron diffraction: theory and applications, Ultramicroscopy 110 (2010) 118–125.
[12] Z. Chen, A.J. D'Alfonso, M. Weyland, D.J. Taplin, S.D. Findlay, L.J. Allen, Absolute scale energy dispersive X-ray analysis in scanning transmission electron microscopy, Ultramicroscopy 157 (2015) 21–26.
[13] B.D. Forbes, A.V. Martin, S.D. Findlay, A.J. D'Alfonso, L.J. Allen, Quantum mechanical model for phonon excitation in electron diffraction and imaging using a Born–Oppenheimer approximation, Phys. Rev. B 82 (2010) 104103.
[14] L.J. Allen, A.J. D'Alfonso, S.D. Findlay, Modelling the inelastic scattering of fast electrons, Ultramicroscopy 151 (2015) 11–22.
[15] W. Burger, M.J. Burge, Digital Image Processing: An Algorithmic Introduction Using Java, Springer, London, 2009.
[16] C. Gammer, V.B. Ozdol, C.H. Liebscher, A.M. Minor, Diffraction contrast imaging using virtual apertures, Ultramicroscopy 155 (2015) 1–10.
[17] X. Li, S.Q. Zheng, K. Egami, D.A. Agard, Y. Cheng, Influence of electron dose rate on electron counting images recorded with the K2 camera, J. Struct. Biol. 184 (2013) 251–260.
[18] R.S. Ruskin, Z. Yu, N. Grigorieff, Quantitative characterization of electron detectors for transmission electron microscopy, J. Struct. Biol. 184 (2013) 385–393.
[19] M.J. Hÿtch, W.M. Stobbs, Quantitative comparison of high resolution TEM images with image simulations, Ultramicroscopy 53 (1994) 191–203.
[20] A. Thust, High-resolution transmission electron microscopy on an absolute contrast scale, Phys. Rev. Lett. 102 (2009) 220801.
[21] J.M. LeBeau, S.D. Findlay, L.J. Allen, S. Stemmer, Quantitative atomic resolution scanning transmission electron microscopy, Phys. Rev. Lett. 100 (2008) 206101.
[22] J.M. LeBeau, A.J. D'Alfonso, S.D. Findlay, S. Stemmer, L.J. Allen, Quantitative comparisons of contrast in experimental and simulated bright-field scanning transmission electron microscopy images, Phys. Rev. B 80 (2009) 174106.
[23] J.M. LeBeau, S. Stemmer, Experimental quantification of annular dark-field images in scanning transmission electron microscopy, Ultramicroscopy 108 (2008) 1653–1658.
[24] C. Dwyer, C. Maunders, C. Zheng, M. Weyland, P.C. Tiemeijer, J. Etheridge, Sub-0.1 nm-resolution quantitative scanning transmission electron microscopy without adjustable parameters, Appl. Phys. Lett. 100 (2012) 191915.
[25] H.-P. Komsa, J. Kotakoski, S. Kurasch, O. Lehtinen, U. Kaiser, A. V. Krasheninnikov, Two-dimensional transition metal dichalcogenides under electron irradiation: defect production and doping, Phys. Rev. Lett. 109 (2012) 035503.
[26] H.G. Brown, A.J. D'Alfonso, Z. Chen, A.J. Morgan, M. Weyland, X. Chang, M. S. Fuhrer, S.D. Findlay, L.J. Allen, Structure retrieval with fast electrons using segmented detectors, Phys. Rev. B 93 (2016) 134116.
[27] S.E. Maccagnano-Zacher, K.A. Mkhoyan, E.J. Kirkland, J. Silcox, Effects of tilt on high-resolution ADF-STEM imaging, Ultramicroscopy 108 (2008) 718–726.
[28] K.A. Mkhoyan, S.E. Maccagnano-Zacher, E.J. Kirkland, J. Silcox, Effects of amorphous layers on ADF-STEM imaging, Ultramicroscopy 108 (2008) 791–803.
[29] J.N. Chapman, P.E. Batson, E.M. Waddell, R.P. Ferrier, The direct determination of magnetic domain wall profiles by differential phase contrast electron microscopy, Ultramicroscopy 3 (1978) 203–214.
[30] N. Shibata, S.D. Findlay, Y. Kohno, H. Sawada, Y. Kondo, Y. Ikuhara, Differential phase-contrast microscopy at atomic resolution, Nat. Phys. 8 (2012) 611–615.
[31] M. Lohr, R. Schregle, M. Jetter, C. Wächter, T. Wunderer, F. Scholz, J. Zweck, Differential phase contrast 2.0-opening new fields for an established technique, Ultramicroscopy 117 (2012) 7–14.
[32] R. Close, Z. Chen, N. Shibata, S.D. Findlay, Towards quantitative, atomic-resolution reconstruction of the electrostatic potential via differential phase contrast using electrons, Ultramicroscopy 159 (2015) 124–137.
[33] A. Lubk, J. Zweck, Differential phase contrast: an integral perspective, Phys. Rev. A 91 (2015) 023805.
[34] A. Lubk, A. Béché, J. Verbeeck, Electron microscopy of probability currents at atomic resolution, Phys. Rev. Lett. 115 (2015) 176101.
[35] E.M. Waddell, J.N. Chapman, Linear imaging of strong phase objects using asymmetrical detectors in STEM, Optik 54 (1979) 83–96.
[36] J.M. Rodenburg, Ptychography and related diffractive imaging methods, Adv. Imaging Electron Phys. 150 (2008) 87–184.
[37] A.M. Maiden, J.M. Rodenburg, An improved ptychographical phase retrieval algorithm for diffractive imaging, Ultramicroscopy 109 (2009) 1256–1262.
[38] A.J. D'Alfonso, A.J. Morgan, A.W.C. Yan, P. Wang, H. Sawada, A.I. Kirkland, L. J. Allen, Deterministic electron ptychography at atomic resolution, Phys. Rev. B 89 (2014) 064101.
[39] C. Dwyer, R. Erni, J. Etheridge, Method to measure spatial coherence of subangstrom electron beams, Appl. Phys. Lett. 93 (2008) 021115.
[40] P. Schlossmacher, D.O. Klenov, B. Freitag, H.S. Von Harrach, Enhanced detection sensitivity with a new windowless XEDS system for AEM based on silicon drift detector technology, Microsc. Today 18 (2010) 14–20.
[41] M.W. Tate, P. Purohit, D. Chamberlain, K.X. Nguyen, R.M. Hovden, C.S. Chang, P. Deb, E. Turgut, J.T. Heron, D.G. Schlom, D.C. Ralph, G.D. Fuchs, K.S. Shanks, H. T. Philipp, D.A. Muller, S.M. Gruner, High dynamic range pixel array detector for scanning transmission electron microscopy, Microsc. Microanal. 22 (2016) 237–249.
[42] G. McMullan, S. Chen, R. Henderson, A.R. Faruqi, Detective quantum efficiency of electron area detectors in electron microscopy, Ultramicroscopy 109 (2009) 1126–1143.
[43] M.C. Sarahan, M. Chi, D.J. Masiel, N.D. Browning, Point defect characterization in HAADF-STEM images using multivariate statistical analysis, Ultramicroscopy 111 (2011) 251–257.

[44] A. Belianinov, R. Vasudevan, E. Strelcov, C. Steed, S.M. Yang, A. Tselev, S. Jesse, M. Biegalski, G. Shipman, C. Symons, A. Borisevich, R. Archibald, S. Kalinin, Big data and deep data in scanning and electron microscopies: deriving functionality from multidimensional data sets, Adv. Struct. Chem. Imaging 1 (2015) 1–25.
[45] R.B. Cattell, The scree test for the number of factors, Multivar. Behav. Res. 1 (1966) 245–276.
[46] S. Jesse, M. Chi, A. Belianinov, C. Beekman, S. Kalinin, A. Borisevich, A. Lupini, Big data analytics for scanning transmission electron microscopy ptychography, Sci. Rep. 6 (2016) 26348.
[47] G. Möbus, M. Rühle, Structure determination of metal-ceramic interfaces by numerical contrast evaluation of HRTEM micrographs, Ultramicroscopy 56 (1) (1994) 54–70.